Meso-scale modelling of FRP-to-concrete bond interfaces

Yaqi Li[a], Esmaeel Esmaeeli[b], Wei Sha[c], ZhenJun Yang[a]*, Jian-Fei Chen[d]*

[a] Hubei Key Lab of Geotechnical and Structural Safety, School of Civil Engineering, Wuhan University, Wuhan 430072, China

[b] Department of Civil and Environmental Engineering, Brunel University London, London UB8 3PH, UK

[c] School of Natural and Built Environment, Queen's University Belfast, Belfast BT9 5AG, UK

[d] Department of Ocean Science and Engineering, Southern University of Science and Technology, Shenzhen 518000, China

*Corresponding author: zhjyang@whu.edu.cn, chenjf3@sustech.edu.cn

Abstract

The bond behaviour between fiber-reinforced polymer (FRP) and concrete plays a critical role in the performance of FRP-strengthened reinforced concrete (RC) structures. While extensive research has been conducted on debonding failures, existing studies predominantly treat concrete as homogeneous, neglecting its inherent heterogeneity. This paper proposes an effective meso-scale finite element (FE) model incorporating random aggregate distributions to explicitly account for the heterogeneous nature of concrete. As only the compressive strength of concrete is usually reported in bond tests, a set of equations are identified as a guideline for calculating the material properties of mortar and coarse aggregates, as required by the damage plasticity constitutive relations of materials which are employed to model both coarse aggregates and mortar. The proposed model is validated through simulations of uniaxial tensile and compressive tests of concrete and FRP-to-concrete bonded joint experiments. Results demonstrate that the model's capability to predict the mesoscopic damage and fracture evolution, as well as the macroscopic load-displacement curves and failure patterns. A parametric study reveals that increasing the coarse aggregate fraction from 30% to 50% enhances bond strength and displacement by 7–8%. This meso-scale approach provides a robust tool for developing bond strength and bond-slip models, incorporating concrete's meso-structural characteristics.

Keywords: Fiber reinforced polymer (FRP); Concrete; Bond behaviour; Meso-scale modelling; Monte Carlo simulation

1. Introduction

Fibre reinforced polymer (FRP) composites are widely used for strengthening or retrofitting concrete structures, due to their advantages such as high strength-to-weight ratio, superior resistance to environmental attacks, good fatigue properties and ease of installation [1]. The main form of FRP strengthening is the bonding of thin FRP laminates to the surfaces of structural elements. The effectiveness of this strengthening technique is largely dependent upon the bond behaviour between the concrete and the FRP [2]. Existing experimental studies have shown that the ultimate strength of FRP in FRP strengthened structures cannot usually be achieved due to FRP debonding failures [3,4]. As a result, the concrete-FRP bond behaviour has attracted extensive experimental research efforts, using both beams [5–7] and FRP-to-concrete bonded joints [8–11] as classified by Chen *et al.*[12] and Yao *et al.* [8]. Numerical simulations of the FRP-to-concrete bond behaviour have also been undertaken, predominantly in 2D [13,14], and very limitedly in 3D, to consider the effect of the FRP width [15,16].

In the FRP-to-concrete bonded joint test, an FRP strip (either prefabricated plate or wet-layup sheet) is bonded onto a concrete prism. When the FRP is debonded from a normal strength concrete substrate, a thin layer (about 2-5 mm) of concrete is usually attached to the FRP, so the failure actually occurs in the concrete in most cases and the mechanical properties of this layer of concrete shall have dominant effects on the bond behaviour. It is thus reasonable to expect that the composition of concrete near the surface affects the bond behaviour. Limited experimental studies have been conducted to investigate the effect of concrete heterogeneity on the FRP-to-concrete bond behaviour. Pan *et al.* [17] found that the bond capacity is highly affected by the interfacial friction due to aggregate interlocking, and the distribution and volume fraction of coarse aggregates on the bond surface. Mostofinejad *et al.* [18] investigated the effect of the volume proportion of fine aggregates in total aggregates, using the single shear test, and found that as more fine aggregates were used, the bond strength was first reduced (when the proportion of fine aggregate was between 0.3 and 0.6) and then increased (when the proportion of fine aggregate was between 0.6 and 1.0). Mukhtar [19] investigated the influence of coarse aggregate properties and found that the specimens containing 30% steel slag aggregates by weight show improved bond performance compared with normal aggregates. A previous paper of the authors [20] on beam tests found that the presence of coarse aggregates on the FRP-concrete joint leads to 19% higher bond strength, but much higher variations in the bond strength and the strain distribution across the width of FRP sheets, than the FRP-mortar joints.

These limited experimental investigations indicate that both the mechanical properties and the composition of concrete can affect the performance of FRP-to-concrete bond interfaces. To capture the stochastic nature, a large number of specimens have to be used which makes experimental investigation very expensive. Numerical simulations can thus play a major role because once validated, a large number of digital samples can be generated, and extensive parametric studies can be conducted with ease for statistical information and analysis.

However, nearly all existing numerical models of FRP-to-concrete bond interfaces are macroscopic in nature, assuming homogeneous material behaviour. In contrast, meso-scale modelling can explicitly incorporate the meso-structure of concrete, allowing for a more realistic simulation of the complicated heterogeneity and stochastic mechanical behaviour due to the varying shapes, sizes and random distributions of coarse aggregates, and thus enables more realistic analysis of stress concentrations and crack paths that arise due to aggregate interactions.

This paper presents a numerical method considering the heterogeneous nature of concrete, using an effective *meso-scale* finite element (FE) model with randomly generated coarse aggregates. A 2D *meso-scale* modelling framework is first proposed, describing the generation of a 2D stochastic mesoscopic FE model and the determination of material properties for the meso-components of concrete. Validations against benchmark tests and parametric analyses demonstrate the model's ability to capture meso-scale damage mechanisms and predict macroscopic bond behaviour.

2. Meso-scale concrete finite element model

2.1 Generation of concrete meso-structure

At the *meso-scale*, concrete has mainly two components: coarse aggregates and mortar. There are two common approaches to generate the meso-structure: the digital image-based approach which generates the coarse aggregate distribution using digital images (usually from micro-XCT scans), and the computer-generation approach. In this work, the latter is adopted because it can generate a large number of random samples with little cost. A “take-and-place” algorithm is adopted and implemented in

MATLAB to generate randomly distributed aggregates and the remaining space is filled with mortar. The procedure is that an aggregate of random size and shape is generated according to a given size grading curve. Then random numbers are generated to define the position of the aggregate. An intersection detection algorithm between this aggregate and existing ones is conducted before the placement of each aggregate. If intersection or overlapping is detected, this aggregate is disregarded and a new set of random numbers are generated to produce a new one in a new position. This process is repeated until the target total aggregate area is achieved. The detailed procedure is widely available [21] and is not repeated here. In this study, polygons with 4 to 8 edges are used to represent crushed stone aggregates.

Fig. 1 shows two *meso-scale* samples generated according to one of the aggregate sieve tests in Hirsh [22] which is given in Table 1. The coarse aggregate area ratio is 40% and the remaining areas represent the mortar. A key aspect of the generation process is establishing a cut-off size to distinguish between coarse and fine aggregates. The maximum size for fine aggregates is usually (as in this study) set at 2.36 mm when constructing concrete meso-structures[23–25], as particles below this size are difficult to be identified in digitized images [26]. Aggregates and cement particles smaller than 2.36 mm are typically not modelled individually but are instead treated as part of the mortar matrix. This approach maintains model fidelity while avoiding the computational challenges associated with simulating a large number of tiny elements, which would significantly increase both processing time and model complexity.

It should be noted that the interfacial transitional zones (ITZ) between the aggregates and mortar are not explicitly modelled in this study, because the thickness of the ITZ is typically 10-50 μm [27], and including such a thin layer of elements in a *meso-scale* model leads to very fine meshes and numerical difficulties [28]. The material properties of ITZ are also not readily available – which makes it difficult to use interfacial elements such as cohesive or contact elements for the ITZ.

Table 1 Size grading of coarse aggregates [22]

Sieve size (mm)	Total percentage passing (%)
12.7	100
9.5	77
4.75	26
2.36	0

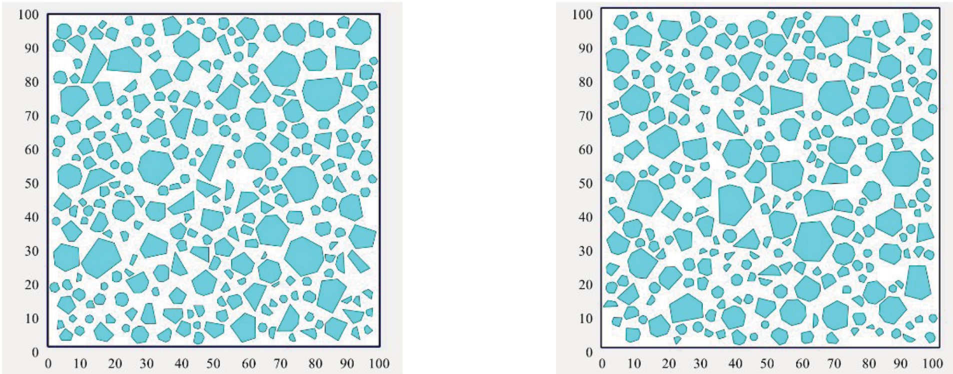

Fig. 1. Computer generated 100 mm square meso-scale concrete samples

2.2 Determination of basic material properties of aggregates and mortar

In many studies, only the standard compressive test strength of concrete is available. The material properties of aggregates and mortar are rarely reported, but they are essential for meso-scale modelling. They are determined as follows in this study.

If the cubic compressive strength of a concrete is f_c for a normal strength concrete, its cylinder compressive strength f_c' can be estimated from $f'_c = 0.79 f_c$ according to BS 8110 [29] and elastic modulus following Eurocode 2 [30]:

$$E_c = 22\left(f_c/10\right)^{0.3} \tag{1}$$

Eq. 1 is also used to estimate the elastic modulus of coarse aggregates E_a in this study.

The elastic modulus of mortar E_m can be estimated using the Mori-Tanaka homogenisation theory [31,32]

$$E_c = E_m + \frac{V_a(E_a - E_m)}{1+(1-V_a)\frac{E_a-E_m}{E_m+4G_m/3}} \tag{2}$$

where V_a is the volume fraction of coarse aggregates; $G_m = \frac{E_m}{2(1+\nu_m)}$ is the shear modulus of the mortar; and ν_m is the Poisson's ratio of the mortar.

The cylinder compressive strength of mortar f_m' is evaluated according to the experimental relationship proposed by Sideris *et al.* [33]

$$f'_m = (E_m - 12.4147)/0.2964 \tag{3}$$

The basic tensile properties are calculated according to the CEB-FIP (1990) model code [34]. The uniaxial tensile strength f_t for the assumed homogeneous concrete and coarse aggregates is:

$$f_t = 1.4\left(\frac{f'_c - 8}{10}\right)^{\frac{2}{3}} \tag{4}$$

The lower bound value of this model is used for the mortar considering its normally lower tensile strength than concrete:

$$f_t = 0.95\left(\frac{f'_c - 8}{10}\right)^{\frac{2}{3}} \tag{5}$$

The Mode I (tensile) fracture energy G_f is [13]

$$G_f = \left(0.0469 d_a^2 - 0.5 d_a + 26\right)\left(\frac{f'_c}{10}\right)^{0.7} \tag{6}$$

where d_a is the maximum aggregate size. In this study the mortar consists of the cement paste and fine aggregates smaller than 2.36 mm. Thus, d_a is assumed to be 2.36 mm when calculating G_f for the mortar. The maximum fracture energy (0.205 N/mm) for C100 concrete in CEB-FIP (1990) model code is adopted for coarse aggregate considering that there is no conventional model for aggregates in concrete.

It can be seen once f_c (or f_t), f_a, v_m and V_a are known, all the other basic material parameters for coarse aggregates and mortar can be calculated using Eqs. 1-6. For normal strength concrete, the uniaxial compressive strength of coarse aggregates f_a' ranges from 80 (for limestones) to 100 MPa (for basalt). Herein f_a'=100 MPa and f_a=123 MPa ([35]) are used in all the simulations in this study. Thus, elastic modulus E_a=46.7 GPa and tensile strength f_t=6.15 MPa for coarse aggregates. The Poisson's ratio is assumed to be 0.2 for both aggregates and mortar. The coarse aggregate volume ratio is usually not reported but it is typically 30–50%. Thus, a coarse aggregates area fraction of V_a=40% is used in all the *meso-scale* models in this paper unless otherwise stated.

2.3 Material properties in the concrete damage plasticity model

The concrete damage plasticity (CDP) model in ABAQUS[36] is used to model the damage and fracture behaviour of both aggregates and mortar. The CDP model has been proven capable of simulating the debonding behaviour in macroscopic models of FRP-to-concrete bond joints [13], as well as mesoscopic concrete fracture behaviour under both static and dynamic loadings [37].

The tensile behaviour of both materials is modelled by the normal traction (σ_t) *vs* crack opening displacement (w_t) relationship proposed by Hordijk [38]:

$$\frac{\sigma_t}{f_t} = \left[1 + \left(c_1 \frac{w_t}{w_{cr}}\right)^3\right] e^{\left(-c_2 \frac{w_t}{w_{cr}}\right)} - \frac{w_t}{w_{cr}}(1 + c_1^3) \tag{7}$$

$$w_{cr} = 5.14 \frac{G_f}{f_t} \tag{8}$$

where w_{cr} is the crack opening displacement at the complete loss of tensile strength, and c_1 = 3.0 and c_2 = 6.93 are constants.

Many compressive stress-strain curves are available for concrete. The following curve proposed by Saenz [39] is used here for both coarse aggregates and mortar

$$\sigma_c = \frac{E_0 \varepsilon_c}{1 + \left(\frac{E_0 \varepsilon_p}{\sigma_p} - 2\right)\left(\frac{\varepsilon_c}{\varepsilon_p}\right) + \left(\frac{\varepsilon_c}{\varepsilon_p}\right)^2} \tag{9}$$

where σ_c and ε_c are the compressive stress and strain, and σ_p and ε_p are the peak stress and the corresponding strain, respectively, σ_p is the cylinder compressive strength (=f'_m for mortar and f'_a for aggregates) and E_0 is the elastic modulus (= E_m for mortar and E_a for aggregates).

It is now widely accepted that the tensile fracture of concrete is localised and should be modelled using the traction-crack opening displacement curves (Eqs. 7-8) with a constant fracture energy G_f, rather than the tensile stress-strain curves, to avoid mesh dependence of results when the continuum mechanics-based CDP model is used ([13]). It is increasingly recognised that the compressive failure process of concrete is also highly localised [40,41], and a similar approach should be used to model damage and crushing in concrete under compression (e.g. [14,42–46]). Specifically, compressive fracture energy or crushing energy G_c [47], is defined similarly to the tensile fracture energy as a material property and the stress-strain curve is adjusted with the mesh size as follows

$$\int \sigma d\varepsilon_{in} = \frac{G_c}{h_c} \quad (10)$$

where σ - ε_{in} is the stress-inelastic strain curve used in the CDP model, which is adjusted with the characteristic length h_c of each finite element. This is achieved by maintaining the stress value and only changing the inelastic strain of the Saenz [39] curve (Eq. 9) to ensure that the area under the curve is equal to G_c/h_c so that the crushing energy G_c remains a constant material property for any mesh size. From uniaxial compression tests, the crushing energy G_c is 50~100G_f in Vonk [42] and 250G_f in Nakamura and Higai [45]) for normal strength concrete. As no data are available for aggregates and mortar, G_c=150G_f is assumed for both meso-components.

After entering the softening stage, the damage factor under uniaxial tension or compression for both aggregates and mortar is calculated by the Lubliner *et al.*'s (1989) model [48] to represent stiffness degradation

$$d = 1 - \frac{\sigma}{f} \quad (11)$$

in which σ is the stress and f is either the tensile or compressive strength of the material as appropriate.

The plasticity behaviour of the CDP model involves five other parameters: the dilation angle ψ, the flow potential eccentricity ϵ, the ratio of initial biaxial compressive yield stress to initial uniaxial compressive yield stress σ_{b0}/σ_{c0}, the ratio of the second stress invariant on the tensile meridian to that on the compressive meridian K_c and the viscosity regularisation factor μ. The value of ψ for normal strength concrete varies from 30° to 38° in the literature and ψ = 37° is used in this study. The viscoplastic regularisation factor μ is used to overcome severe convergence difficulties due to softening behaviour and stiffness degradation of materials. A higher value tends to speed up convergence but reduce the accuracy of the results. A sensitivity analysis was conducted and the results showed that $\mu = 10^{-6}$ is suitable for both convergence and accuracy. Default values in ABAQUS are used for the other three parameters: $\epsilon = 0.1$, $\sigma_{b0}/\sigma_{c0} = 1.16$ and $K_c = 0.667$.

3. Validation

The *meso-scale* concrete modelling approach proposed above was validated by simulating benchmark tests of uniaxial tension, uniaxial compression and a single shear FRP-to-concrete bonded joint, before it was applied to a wide range of FRP-to-concrete bonded joint shear tests from various sources.

3.1 Uniaxial tension test

The square specimen HS06 of 100 mm size with two middle notches on the left and right edges tested by Li and Absari [49] was simulated first to validate the proposed meso-scale modelling approach. The generated *meso-scale* FE mesh is shown in Fig. 2. All materials were modelled using the 4-node plane stress element (CPS4) with a global mesh seed of 1 mm. The boundary condition is also shown. All the nodes at the upper boundary are subjected to a uniform vertical displacement. The reported concrete tensile strength f_t in [49] was 3.2 MPa. All the properties of the mortar were calculated according to the equations in Section 2.2: elastic modulus E_m = 31 GPa, compressive cylinder strength f_m' = 62.6 MPa, tensile strength f_t = 2.95 MPa and fracture energy G_f = 0.091 N/mm.

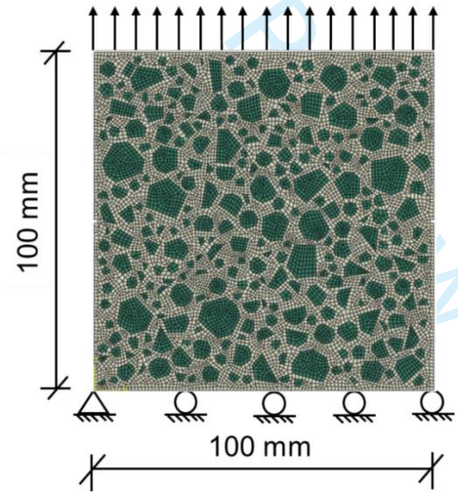

Fig. 2. A *meso-scale* numerical model under uniaxial tension

Fig. 3 compares the simulated stress-strain curves for three mesh sizes (2 mm, 1.5 mm and 1 mm) and the test data. Although the prediction of the 2 mm mesh appears to be closer to the test results, those from the 1.5 mm and 1 mm meshes are almost the same thus it may be appropriate to state that mesh convergence was obtained at 1.5 mm. Monte Carlo simulations of 10 *meso-scale* samples with different distributions of coarse aggregate were carried out using meshes of 1 mm element size. The 10 stress-strain curves together with their mean are plotted in Fig. 4. It is seen that the curves are close to the experimental data. The randomness of the coarse aggregate distribution has little effect on the tensile peak stress (strength). Its main effect is on the softening branch.

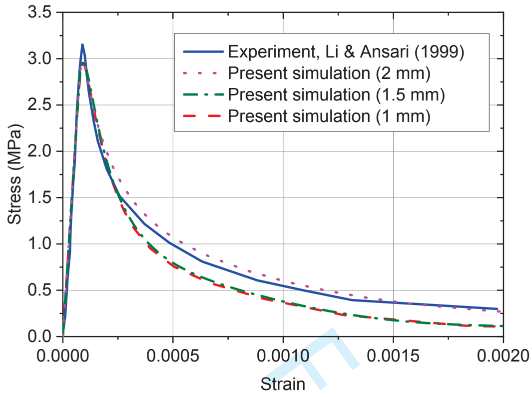

Fig. 3. Stress-strain curves of the uniaxial tension test

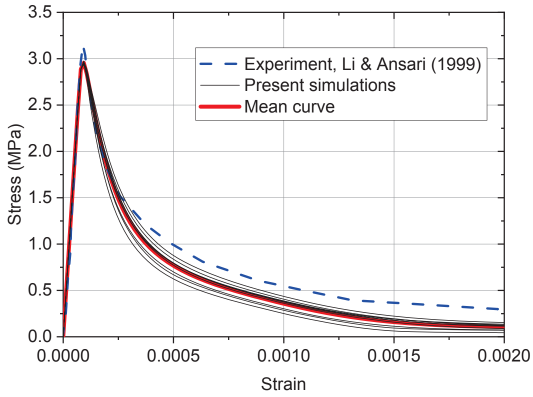

Fig. 4. Stress-strain curves for 10 samples of the uniaxial tension test

Fig. 5 shows the damage and fracture process in the *meso-scale* model shown in Fig. 2, where the elements with high values of tensile damage index DAMAGET (normally DAMAGET ≥ 0.8) can be regarded as cracks [28]. Little damage is seen before the peak stress with a corresponding strain of about 90με. Damage initiates first in the mortar near the aggregate-mortar interfaces shortly after the peak stress (Fig. 5(a)). After the peak, the damage index increases and the damaged areas extend, to form a highly localised macroscopic crack. This is similar to the results from continuum-based simulations with the ITZ modelled [28,50] or discrete crack based simulations using cohesive elements for the mortar-aggregate interfaces [21,51,52].

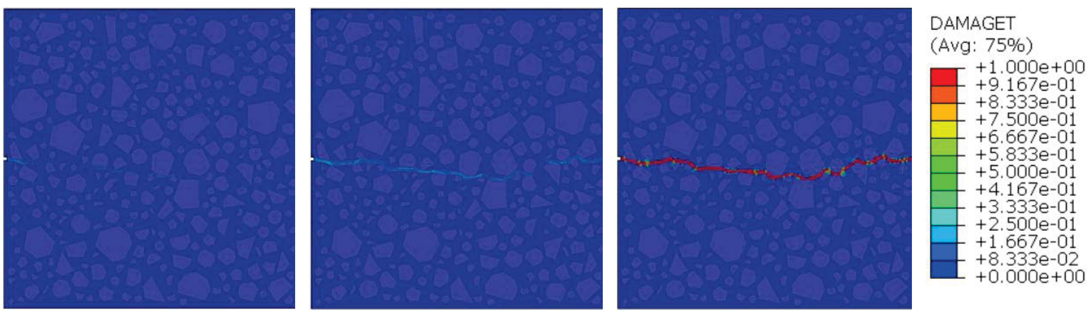

(a) Strain = 100με (immediately after peak stress)

(b) Strain = 150με

(c) Strain = 2000με

Fig. 5. Crack propagation in the mesoscopic uniaxial tension test

3.2 Uniaxial compression tests

A 100 mm concrete cube tested by van Mier [41] under uniaxial compression was next modelled. Fig. 6 shows a 2D *meso-scale* sample with a global mesh seed of 1 mm. The model is sandwiched between two rigid plates; the lower plate is fixed while the upper one moves downwards to compress the specimen. Surface-to-surface contact with no friction and a friction coefficient of 0.47 [53] was defined between the concrete and the plates to simulate the effects of the end friction. The reported cubic compressive strength of concrete in [41] is 43 MPa, from which the material properties of mortar were calculated from the equations in Section 2.2 as: $E_m = 27.8$ GPa, $f_m' = 51.9$ MPa, $f_t = 2.55$ MPa and $G_f = 0.079$ N/mm.

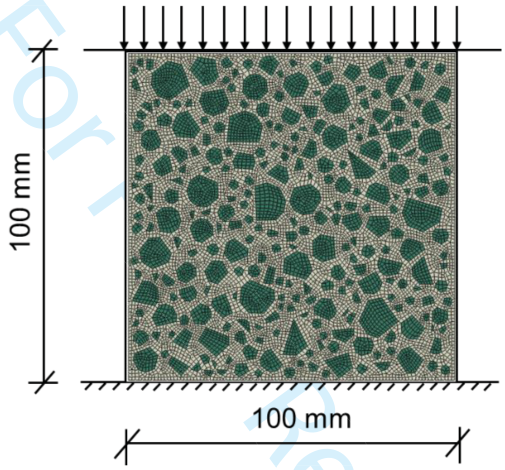

Fig. 6. A meso-scale numerical sample under uniaxial compression

The simulated stress-strain curves with different mesh sizes are shown in Fig. 7, together with the experimental result from [41]. The results are slightly mesh-dependent, indicating the effectiveness of the crushing energy-based method (Eq. 10), particularly for the model with end friction. The numerical results with end friction are much closer to the experimental data than those without end friction, because the former is better in line with the experimental setting. Monte Carlo simulations of 10 *meso-scale* numerical samples with end friction were also carried out for the uniaxial compression test, and the results are shown in Fig. 8. The predicted mean strength is 43.8 MPa, very close to the experimental value of 43.2 MPa.

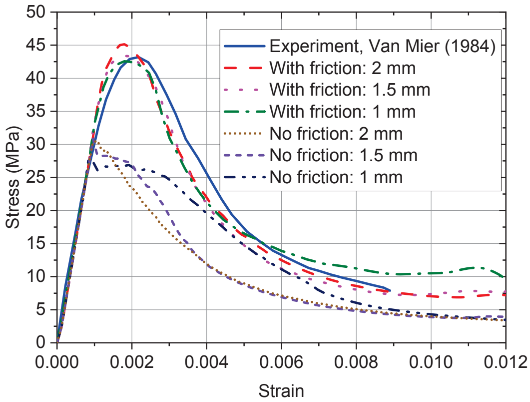

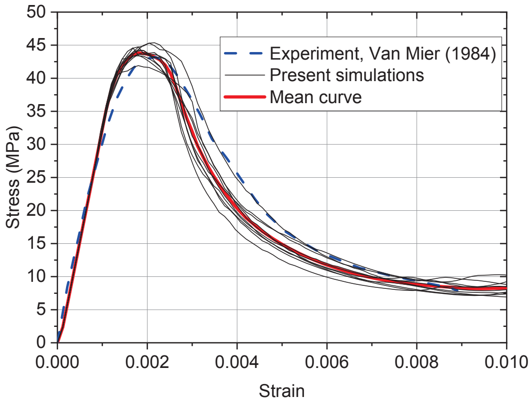

Fig. 7. Stress-strain curves of the uniaxial compression test

Fig. 8. Stress-strain curves for 10 samples of the uniaxial compression test with end friction

The damage evolution processes of the *meso-scale* model with and without end friction are shown in Fig. 9, where the damage is represented by the overall stiffness degradation index SDEG. It can be seen that the failure mode with end friction is the typical cone failure with X-shaped localised shear cracks, whereas the model without end friction fails with diffusive cracks parallel or slightly inclined to the loading direction and uniform dilatation [50,54].

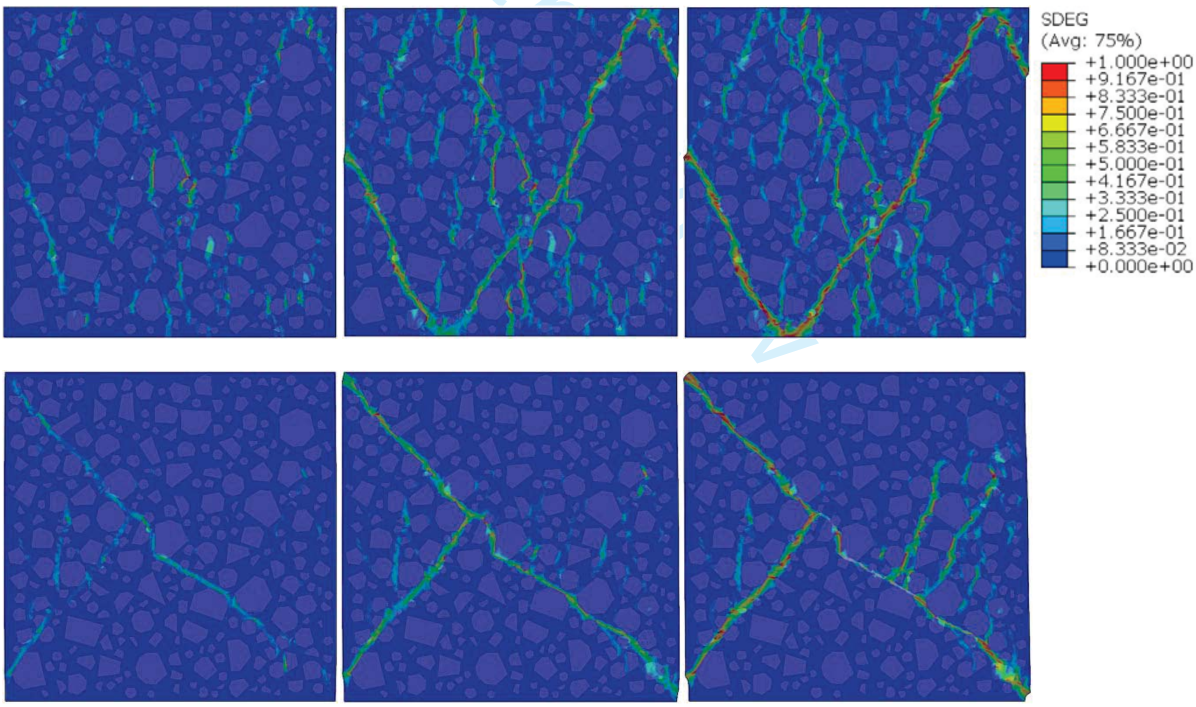

Strain = 0.003 Strain = 0.006 Strain = 0.012

Fig. 9. Effect of boundary friction on uniaxial compression (top row: no friction; bottom row: friction coefficient = 0.47)

3.3 Single shear test of an FRP-to-concrete bonded joint

3.3.1 The FE Model

The FRP-to-concrete bond behaviour is commonly tested using the single shear test in which an FRP plate is bonded to a concrete prism and subjected to a tensile force. The specimen II-5 tested by Yao *et al.* [8] was simulated here for further validation of the proposed *meso-scale* modelling approach. Fig.10 shows a 2D *meso-scale* sample with an element size of 1 mm. The FRP plate was 0.165 mm thick and 25 mm wide. The bond length was 190 mm. The geometry and boundary conditions shown in Fig.10 are adopted where the specimen is restrained vertically along the base and horizontally along part of the right edge. The nodes at the right edge of the FRP are subjected to a horizontal displacement loading. The ABAQUS/Implicit solver is used with loading time t to model the quasi-static loading condition. The reported cylinder compressive strength of concrete in [8] is 22.9 MPa, from which all the material properties of mortar were calculated from the equations in Section 2.2: E_m = 22.9 GPa, f_m' = 35.5 MPa, f_t = 1.87 MPa and G_f = 0.061 N/mm. The FRP had a modulus of elasticity of 256 GPa.

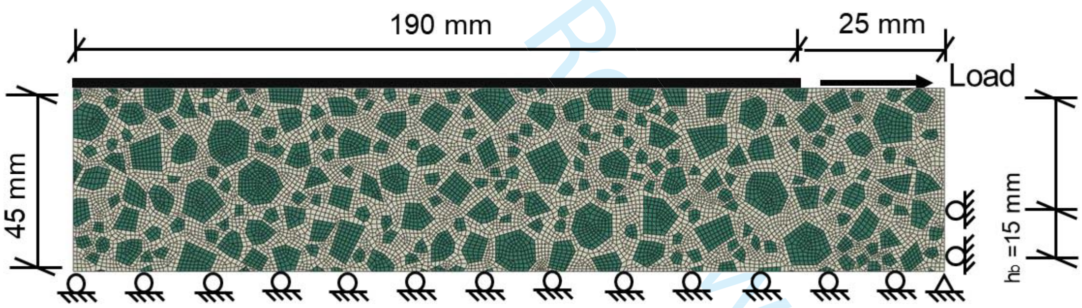

Fig. 10. 2D *meso-scale* FE model of an FRP-to-bonded joint under single shear

The aggregates, mortar and FRP were all modelled using the plane stress element CPS4. Perfect bonding between the FRP plate and concrete was assumed, considering the fact that the strength of the adhesive is generally higher than that of concrete so the debonding failure is usually governed by the concrete cracking under the FRP plate. Because the test was modelled as a plane stress problem while the actual behaviour is three-dimensional due to the different widths of the FRP plate (b_p) and the concrete prism (b_c), a width ratio factor β_w proposed by Chen and Teng [55] was used to correct the responses:

$$\beta_w = \sqrt{\frac{2-b_p/b_c}{1+b_p/b_c}} \qquad (12)$$

All the predictions of load, displacement, stress and strain in the FRP plate were multiplied by the β_w value for the actual b_p and b_c and then divided by β_w value for $b_p = b_c = 1$ mm, as suggested by Li *et al.* [14].

3.3.2 Mesh convergence and effect of loading time

A mesh convergence study was first carried out. Fig. 11 shows the simulated load-displacement (at the loaded end) curves with different mesh sizes together with the experimental results. It can be seen that the differences are negligible between those from the 1 mm and 0.5 mm meshes. Mesh size of 1 mm was used in all the *meso-scale* simulations below, to balance the computational efficiency and accuracy of the predictions. The predicted bond strength (which is defined as the maximum load) with 1 mm mesh is 6.56 kN, close to the experimental value of 7.07 kN.

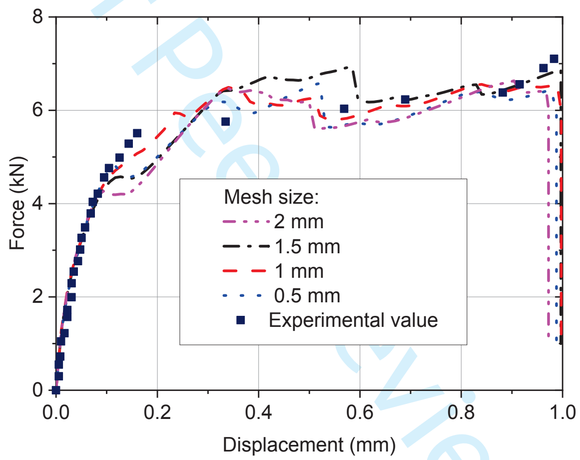

Fig. 11. Load-displacement curves of the single shear test

The *meso-scale* simulations of FRP debonding failures could be very complex because of the presence of highly localised mortar cracking and strong nonlinear bond behaviour between coarse aggregates, mortar and FRP plate, which leads to severe convergence difficulties. Chen *et al.* [56] suggested an implicit dynamic approach to tackle the convergence problem in the FE simulation of FRP-strengthened reinforced concrete beams. The implicit dynamic approach was also adopted in this work. The loading time has a significant effect on the computational efficiency and accuracy of results when the dynamic solver is used to model quasi-static loading conditions. In principle, the loading time must be long enough to minimise any dynamic effects. However, a long loading time results in greater computational costs. So, a balance has to be made between computational efficiency and accuracy.

The calculated fundamental natural period T_1 is 0.00029s for the above bond test model. A parametric study was conducted for comparing the load-displacement curves of the mesoscopic sample with four loading times of 0.003 s, 0.03 s, 0.3 s, and 3 s, which are about 10, 100, 1000, and 10000 times the natural period of the model, respectively. The predicted force-displacement responses at the loaded end of FRP and the corresponding ratios of kinetic energy history to internal energy history are shown in Fig. 12. The running time for models with loading times of 0.003 s, 0.03 s, 0.3 s, 3 s were 5.5 mins, 10.2 mins, 20.0 mins, 66.1 mins, respectively, when conducted by parallel computation using 20 Intel Xeon CPUs E5-2678 @ 2.50 GHz with 1 NVIDIA Quadro P1000 GPU acceleration. It can be seen that the results are almost the same when the loading times are 0.3 s and 3 s. The ratio of kinetic energy to internal energy of t=0.003 s is significantly larger compared to the other three cases, and the models overestimate the ultimate force and the debonding displacement. A loading time of 0.3 s, which is about 1000 times the natural period of the models, was used in the following simulations.

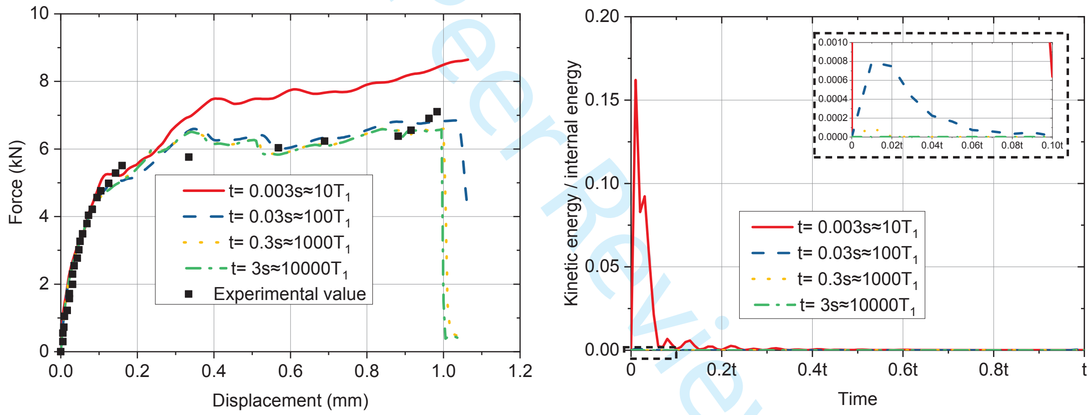

(a) On predicted force-displacement curves (b) On ratio of kinetic energy to internal energy

Fig. 12. Effect of loading time

Fig. 13 shows the damage and fracture process of the *meso-scale* model in Fig. 10. The mortar at the loaded end first exhibits damage and cracking in a small zone under the FRP plate. Then the crack starts to propagate along the FRP-to-concrete bond interface in the mortar. During the debonding stage, inclined micro-cracks gradually form along the edges of coarse aggregates adjacent to the bonded line. The bonded joint fails by the separation of the FRP plate from the concrete, with a thin layer of concrete attached (with mortar and a small number of small coarse aggregates). This debonding process resembles well with the typical FRP debonding failure mode observed in experiments. The fluctuations in the predicted load-displacement curves are caused by the presence of random coarse aggregates and the gradual formation of micro-cracks during the debonding process.

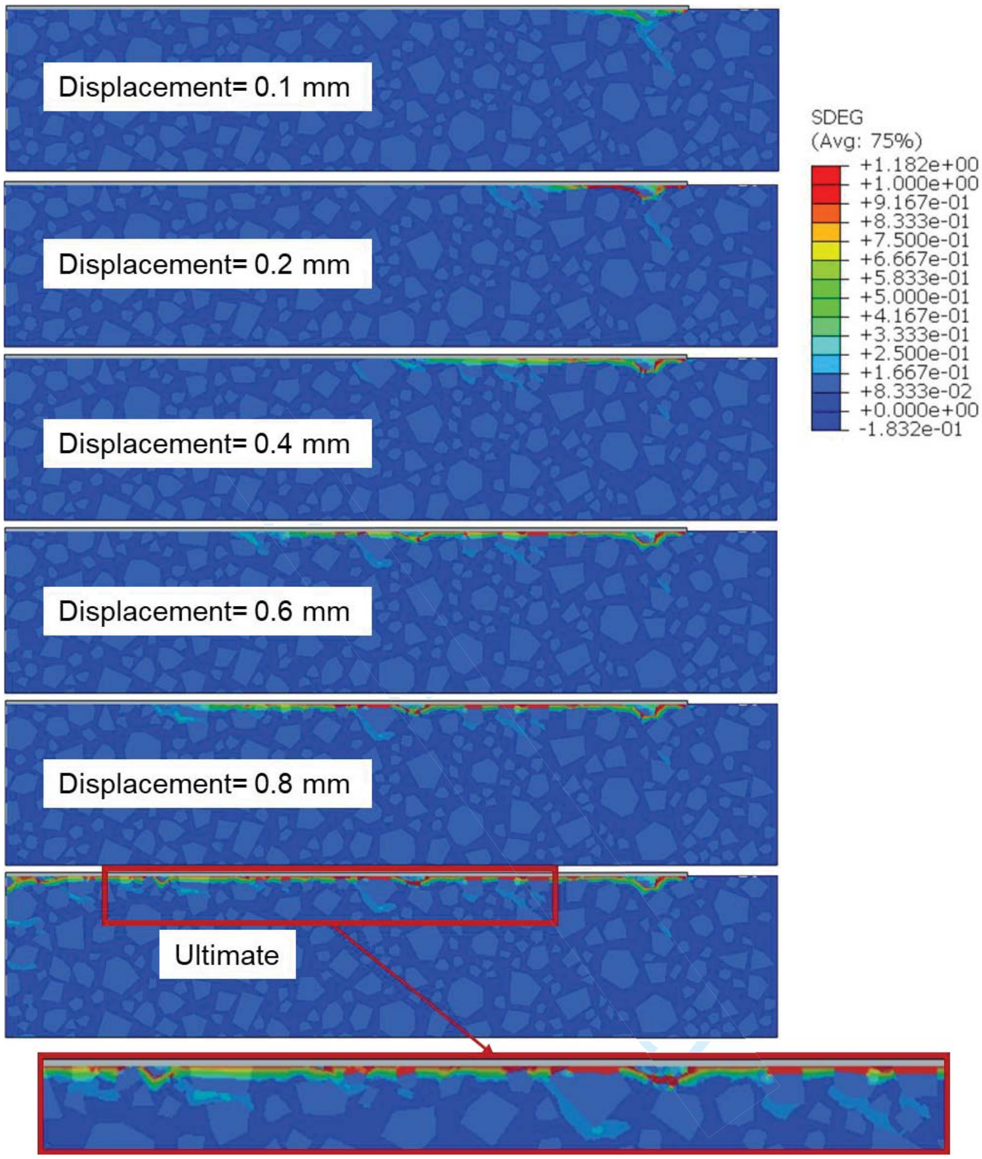

Fig. 13. Failure process of specimen II-5 in Yao *et al.* (2005)

Fig. 14 presents the strain distributions along the upper and lower surfaces of the FRP plate at various loading levels. They show notable local fluctuations consistent with experimental observations [57, 58]. These strain variations can be attributed to localized material heterogeneity, specifically the distribution of coarse aggregates and the resulting local bending of the FRP plate. For examples, the crack above the aggregate at point A and the support from the neighbouring one (circled in yellow) leading to localized downward bending in the FRP plate. As a result, the upper surface of the FRP plate experiences a reduction (Fig. 14a), while the lower surface undergoes an increase (Fig. 14b) of the tensile strains. At point B, a relatively large region is lack of aggregates, causing an upward local bending of the FRP plate.

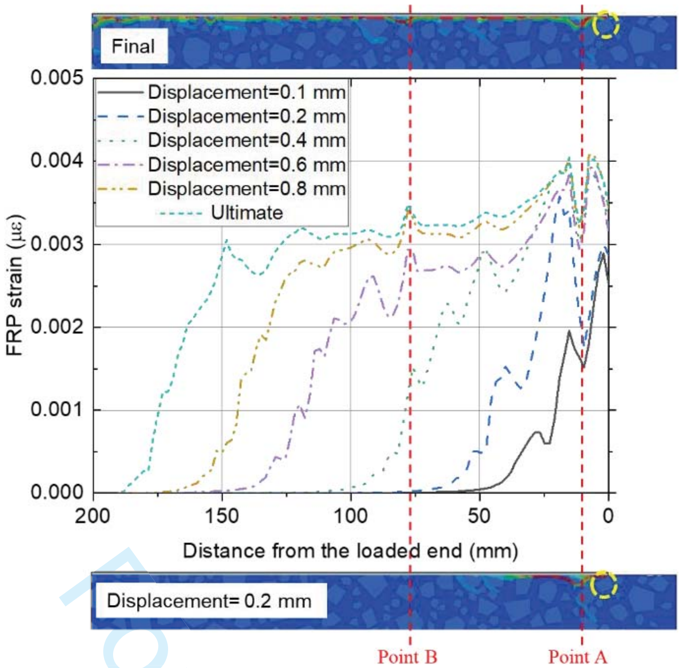

(a) On the upper surface of FRP

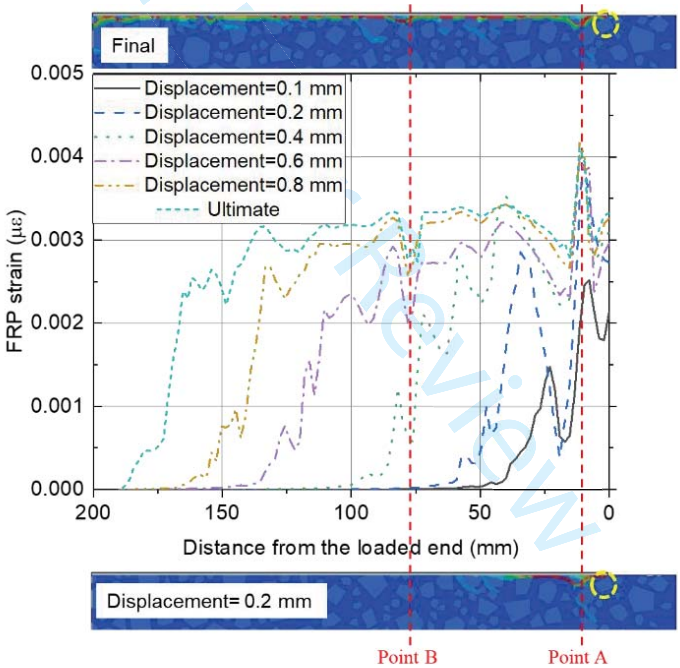

(b) On the lower surface of FRP

Fig. 14. Strain distributions at different loading levels of specimen II-5 in Yao *et al.* (2005)

3.3.3 Effect of damage model

Previous research has indicated that CDP simulations of FRP-to-concrete interface debonding behaviour are sensitive to the damage definition which governs the damage evolution upon unloading. Finding that the Lubliner *et al.*'s model [59] (Eq. 12) is not effective, Tao and Chen [13] proposed a damage definition in CDP models which were effective in simulating the concrete-to-FRP debonding behaviour at macroscale. The review of eight empirical damage models by An [59] found that Birtel and Mark's model [60] provided the best match for the FRP-to-concrete bond strength in macroscopic simulations. The effects of these three damage models in simulating *meso-scale* interfacial debonding of FRP-to-concrete bonded joints are explored here.

In ABAQUS, the concrete damage factor d is used to characterise the stiffness degradation under uniaxial loading:

$$\sigma = (1 - d)E_0(\varepsilon - \varepsilon^{pl}) \tag{13}$$

where E_0 is the initial (undamaged) modulus of elasticity and ε^{pl} is the plastic strain. The concept is illustrated in Fig. 15, in which other strain conventions are also defined.

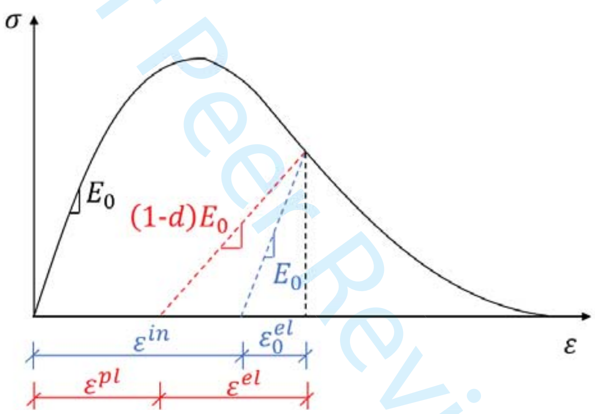

Fig. 15. Damage definition of CDP model in ABAQUS

Birtel and Mark's model [60] defines the damage factor as

$$d = 1 - \frac{\sigma/E}{\varepsilon^{pl}\left(\frac{1}{b}-1\right)+\sigma/E} \tag{14}$$

where b is defined as $\varepsilon^{pl}/\varepsilon^{in}$ and is typically assumed as 0.7.

Eq. 14 can be rewritten as

$$d = \frac{\varepsilon^{in}(1-b)}{\varepsilon^{in}(1-b)+\sigma/E} \tag{15}$$

Tao and Chen's model [13] defines damage as

$$d = \begin{cases} \frac{\varepsilon^{in}(1-c)}{\varepsilon^{in}(1-c)+\sigma/E}, if\ \dot{\bar{\varepsilon}}^{pl} \geq 0 \\ \frac{\varepsilon^{in}-(\varepsilon-\bar{\varepsilon}^{e}_{cr})}{\varepsilon^{in}-(\varepsilon-\bar{\varepsilon}^{e}_{cr})+\sigma/E}, if\ \dot{\bar{\varepsilon}}^{pl} < 0 \end{cases} \tag{16}$$

where $c = \sigma/f$ (see Eq. 9) and $\bar{\varepsilon}^{e}_{cr}$ is the critical elastic strain when the plastic strain rate $\dot{\bar{\varepsilon}}^{pl}$ is zero.

Figs. 16a and 16b compare the three damage curves calculated by Eqs. 11, 15 and 16 for the mortar under compression and tension, respectively, using the material properties in the example in this section. The same models were used for the coarse aggregates. It is seen that the damage evolves with much higher rates in the Birtel and Mark's model [60] and Tao and Chen's model [13] than that in the Lubliner *et al.'s* model [59], especially in tension, because the former two models are mesh dependent where the damage is calculated from the inelastic strain (see Eqs. 15 and 16) equal to the crack width w_t (see Eq. 7) divided by the characteristic element size.

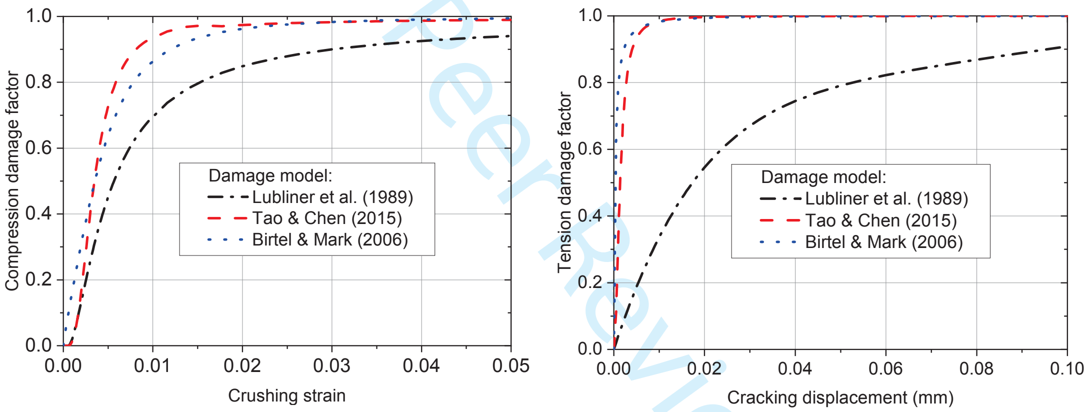

(a) Mortar: under compression (b) Mortar: under tension

Fig. 16. Damage evolution curves of three models for the mortar (1 mm element size)

Fig. 17 shows the simulated load versus displacement curves for the meso-model in Fig. 10 using the three damage models. The simulations using the Birtel and Mark's model and the Tao and Chen's model terminated at an early stage due to convergence difficulties. It can be seen that different damage models lead to significantly different results. The predictions using Lubliner *et al.*'s model appear to be in closer agreement with the test results, whereas Birtel and Mark's model significantly over-predicts the bond strength. The damage models also affect the predicted failure pattern as shown in Fig. 18. Lubliner *et al.*'s model was used in all simulations in the rest of this paper.

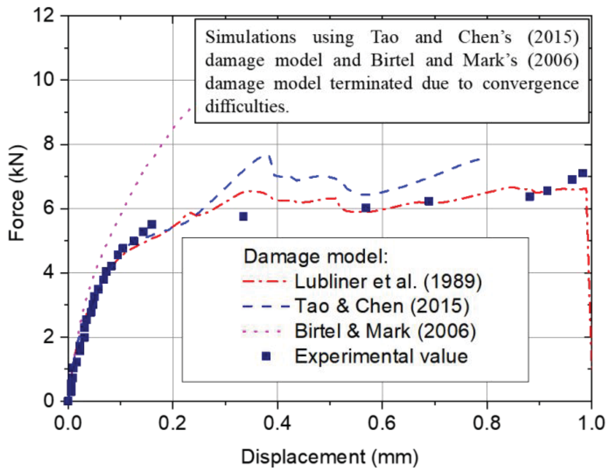

Fig. 17. Effect of damage model on predicted load-displacement curve

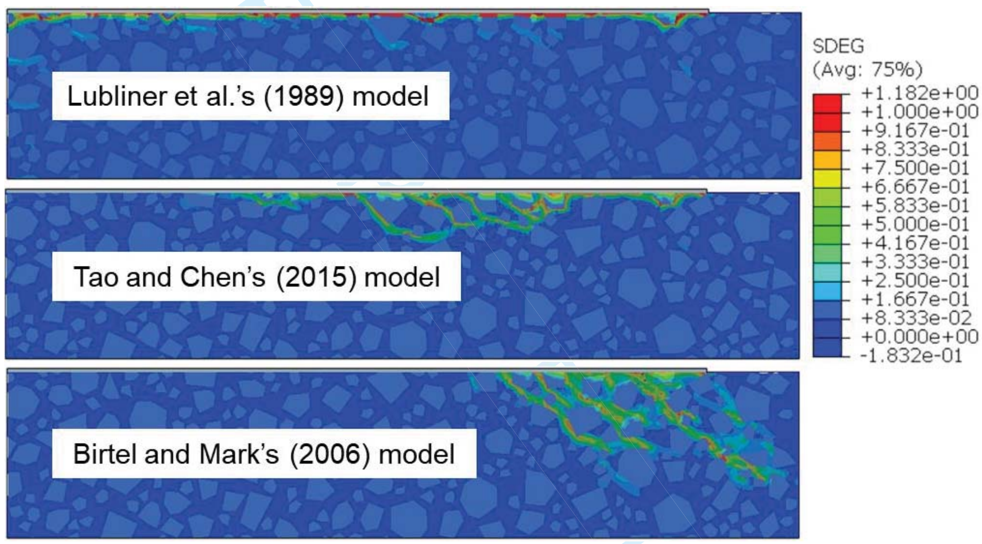

Fig. 18. Effect of damage model on predicted failure pattern

4. Simulation of a set of FRP-to-concrete bonded joint tests

To demonstrate the capability of the proposed 2D mesoscopic FE method, the 56 single shear tests reported in Yao *et al.* [8] were simulated. It may be noted that Yao *et al.* [8] reported a total of 72 tests but 16 of them failed in other modes (concrete prism failure and debonding at the adhesive-concrete interface) rather than debonding in the concrete so they were excluded in this study. These tests used the same geometries and dimensions as in Fig. 10 but with a range of the length and width of the FRP plate and the height of the free concrete edge h_c. For specimens with h_c <= 30 mm, the actual h_c value was used in the simulations here. For specimens with h_c > 30 mm, h_c was set to 30 mm. The cylinder compressive strength of concrete ranged from 18.1 MPa to 24.9 MPa, from which all the material properties of mortar were calculated as listed in Table 2 based on the equations in Section 2.2.

Table 2 Mortar properties for 2D mesoscopic FE simulation for all specimens in Yao *et al.* [8]

Test specimen	Concrete cylinder strength (MPa)	Mortar properties for 2D mesoscopic FE simulation			
		Elastic modulus (GPa)	Compressive strength (MPa)	Tensile strength (MPa)	Fracture energy (N/mm)
Group I	23.0	22.9	35.5	1.87	0.061
Group II	22.9	22.9	35.5	1.87	0.061
Group III	27.1	24.9	42.0	2.15	0.068
Group IV (1)	18.9	21.0	28.8	1.55	0.053
Group IV (2)	19.8	21.4	30.4	1.62	0.055
Group V	21.1	22.1	32.6	1.73	0.057
Group VII	24.9	23.8	38.7	2.01	0.065

To supplement the narrow range of concrete strength in the tests of Yao *et al.* [8], five specimens (No. 1-5) tested in Ali-Ahmad *et al.* [61] and three specimens (S-CFS-400-25) tested in Wu *et al.* [62] were also simulated. The concrete cylinder strength was 38 MPa for the former and 57.6 MPa for the latter. It is noted that in Ali-Ahmad *et al.* [61], the concrete compressive strength test was conducted at 28 days but the debonding tests were conducted at 97 days, so the compressive strength was here increased by 20% as suggested by Guo [63]. The material properties of mortar for these two groups of specimens are listed in Table 3.

Table 3 Mortar properties for 2D mesoscopic FE simulation for specimens in Ali-Ahmad *et al.* [61] and Wu *et al.* [62]

Test specimen	Concrete cylinder strength (MPa)	Mortar properties for 2D mesoscopic FE simulation			
		Elastic modulus (GPa)	Compressive strength (MPa)	Tensile strength (MPa)	Fracture energy (N/mm)
Ali-Ahmad *et al.* [61]	45.6 (97 days)	32.0	66.2	3.08	0.094
Wu *et al.* [62]	57.6	34.5	74.5	3.36	0.102

Fig. 19 compares the test and simulated bond strengths for all the 64 FRP-to-concrete bonded joints. The predictions of Chen and Teng's (2001) [55] model are also shown for reference. It can be seen that both predictions are overall in good agreement with the test data. The present mesoscopic FE model overestimates the bond strength by 4% on average with a coefficient of variation CoV = 12.9% whilst Chen and Teng's analytical model [55] underestimates by 6% on average with CoV = 10.2%. Clearly, both predictions have similar accuracy and scatter when compared with the test results. A plausible reason might be that a constant coarse aggregate grading and volume fraction were used in all the mesoscopic models in this section but these could be different in the test concrete. Furthermore, the distribution of the aggregates is random in nature. This will be further discussed in Section 5.

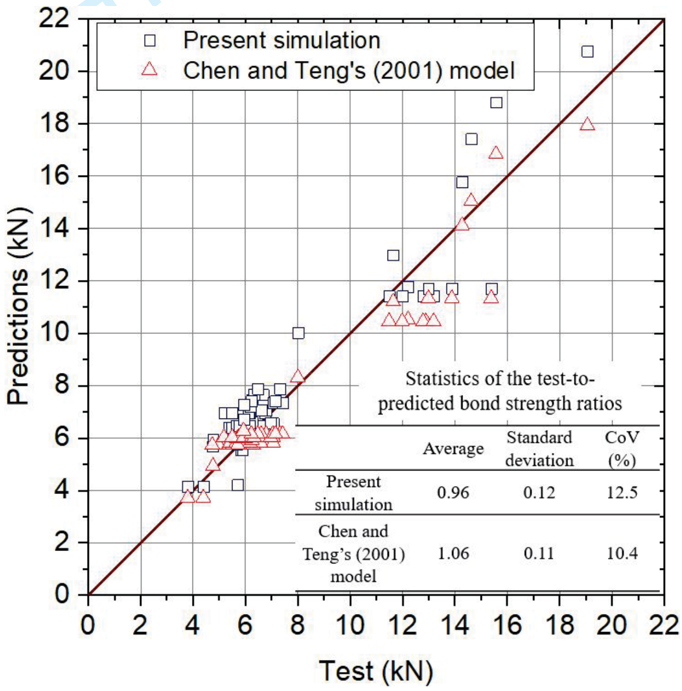

Fig. 19. Comparison of the predicted bond strength of the present simulation with test data

Fig. 20 compares the predicted load-displacement curves from simulations of ten meso-scale random models with the test data in Yao *et al.* [8] and Ali-Ahmad *et al.* [61]. It is seen that the random nature of the coarse aggregate distribution significantly affects the load-displacement responses, as well as the peak force. The predicted bond strength for specimen II-5 in Yao *et al.* [8] ranges from 6.41 to 6.98 kN, slightly lower than the experimental value of 7.07 kN. The predicted strengths for the tests in Ali-Ahmad *et al.* [61] vary from 10.8 kN to 12.2 kN, which are again slightly lower than the five test results between 11.5 kN-13.2 kN.

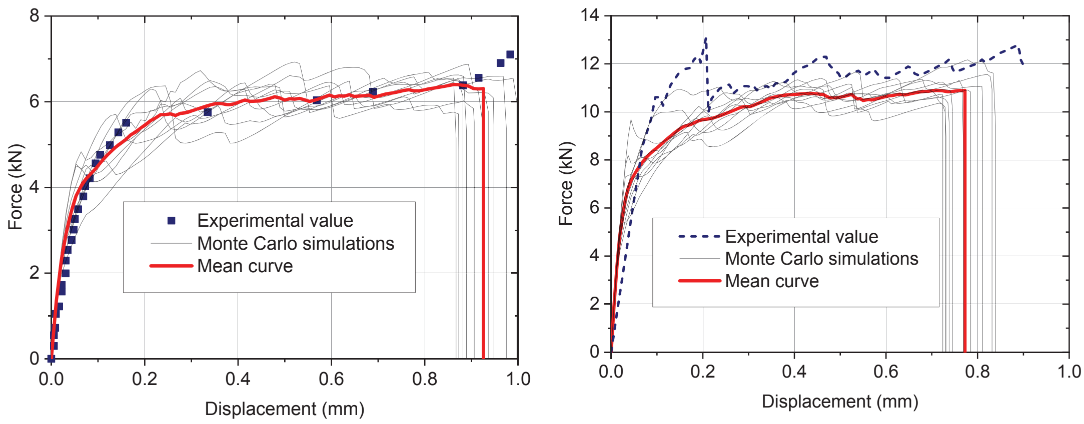

(a) Specimen II-5 in Yao *et al.* [8] (b) Specimens in Ali-Ahmad *et al.* [61]

Fig. 20. Monte Carlo simulations of single shear tests

5. A parametric study

The proposed *meso-scale* modelling approach was adopted for investigating the effect of coarse aggregate area fraction (AF) on the FRP-to-concrete bond behaviour. The single shear test specimen in Ali-Ahmad *et al.* [61] was modelled. Besides AF=40% as presented in Section 4, two additional Monte Carlo simulations with AFs=30% and 50% were carried out, with 10 random *meso-scale* samples generated and simulated for each Monte Carlo simulation. The mesoscopic material properties for the mortar were calculated using f_c'=45.6MPa (97 days) according to the equations in Section 2.2 and listed in Table 4.

Table 4 Mortar properties in 2D mesoscopic FE models for the parametric example (f_c'=45.6MPa)

AF	Mortar properties in 2D mesoscopic FE simulation			
	Elastic modulus (GPa)	Compressive strength (MPa)	Tensile strength (MPa)	Fracture energy (N/mm)
30%	33.8	72.1	3.28	0.100
50%	29.8	58.6	2.80	0.086

The predicted force-displacement curves and the corresponding mean curves of the two additional AFs are shown in Fig. 21. The results for AF=30% and 50% are similar in shape to Fig. 20b with AF=40%. Again, the random aggregate distribution leads to significant scatters in the debonding behaviour. After entering the debonding stage, the mean curve with a higher AF presents a higher peak force as well as the maximum displacement, indicating higher fracture energy of the FRP-to-concrete bonded joint.

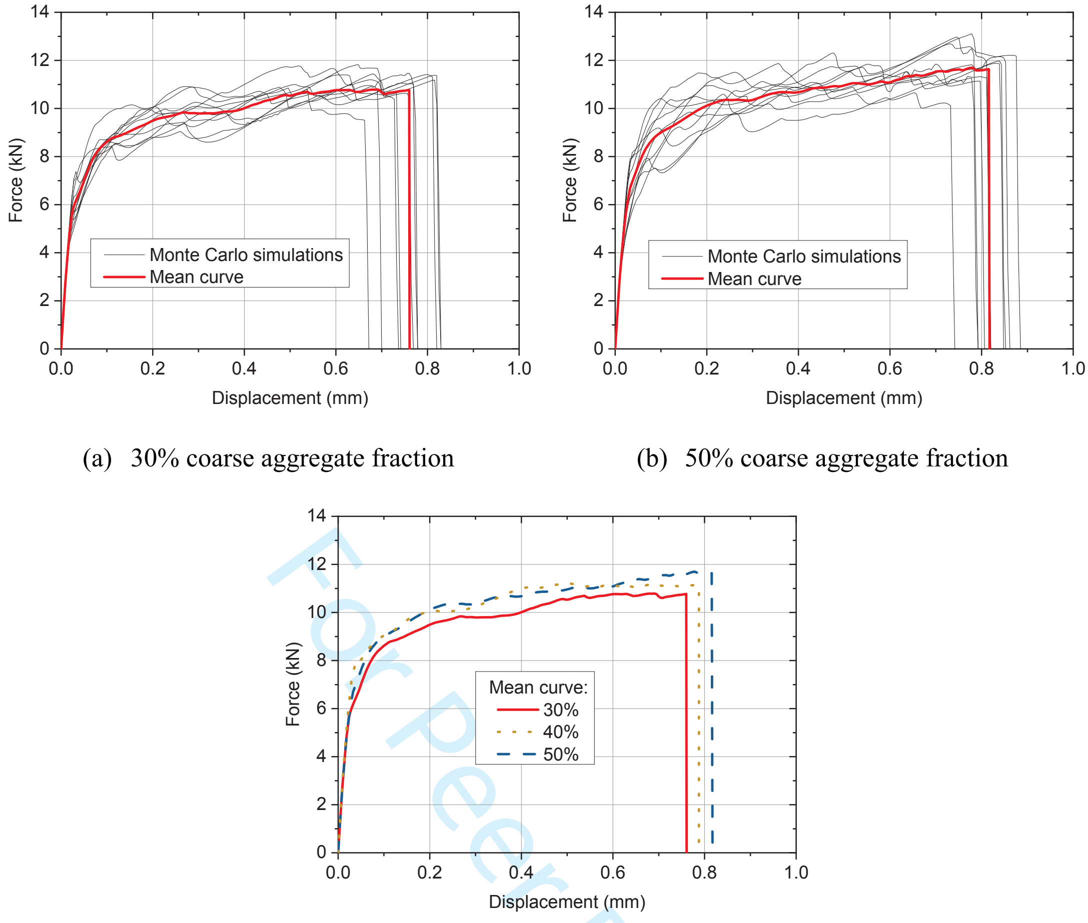

(a) 30% coarse aggregate fraction

(b) 50% coarse aggregate fraction

(c) Comparison

Fig. 21. Monte Carlo simulations with different AFs

Table 5 compares the average peak loads and the average maximum displacements of Monte Carlo simulations with different AFs. When the AF increases from 30% to 50%, both the mean peak load and the final displacement increase by 7~8%, from 11.3 MPa to 12.1 MPa and from 0.76 mm to 0.82 mm, respectively.

Table 5 Average peak load and maximum displacement for different coarse aggregate fractions (AF)

AF	Average peak Load (kN)	Average maximum displacement (mm)
30%	11.3	0.76
40%	11.7	0.79
50%	12.1	0.82

This parametric example shows that the proposed mesoscopic modelling method is capable of investigating the effect of concrete meso-components on the bond behaviour of FRP-to-concrete bonded joints. Extensive parametric studies are being conducted to achieve a better understanding of the bond behaviour.

6. Conclusions

A systematic study on the debonding behaviour of FRP-to-concrete bonded joint has been conducted using *meso-scale* numerical simulations. The main conclusions are:

(1) An efficient algorithm has been developed to generate *meso-scale* models with random coarse aggregates of designed size grading and volume fractions. As only the compressive strength of concrete is usually reported in laboratory test results, a set of equations have been identified for calculating the material properties for both mortar and coarse aggregates required by the concrete damage plasticity (CDP) model.

(2) The *meso-scale* simulations have been successfully validated against uniaxial tensile and compressive benchmark tests and several FRP-to-concrete bonded joint tests from the literature, in terms of load-displacement curves, damage and fracture evolution and failure patterns.

(3) A parametric study has shown that the random distribution of coarse aggregate affects significantly the load-displacement response of FRP-to-concrete bonded joint. When the area fraction of coarse aggregate increases from 30% to 50%, both the mean peak load and the final displacement of the joint increase by 7~8%.

Acknowledgments

This study was partially funded by National Key Research and Development Program of China (2022YFB3706500), the National Natural Science Foundation of China (No. 52173300, 52178218). The work started at Queen's University Belfast when the first author, supported by the China Scholarship Council (CSC), was a PhD student under the supervision of the last author.

References

[1] Teng JG, Chen JF, Simth ST, Lam L. FRP-strengthened RC structures. Chichester: Wiley; 2002.

[2] Chajes MJ, Finch WW, Januszka TF, Thomson TA. Bond and force transfer of composite material plates bonded to concrete. ACI Struct J 1996;93:208–17.

[3] Kang THK, Howell J, Kim S, Lee DJ. A State-of-the-Art Review on Debonding Failures of FRP Laminates Externally Adhered to Concrete. Int J Concr Struct Mater 2012;6:123–34.

[4] Teng JG, Chen JF. Mechanics of debonding in FRP-plated RC beams. Proceedings of the Institution of Civil Engineers: Structures and Buildings 2009;162:335–45.

[5] Gartner A, Douglas EP, Dolan CW, Hamilton HR. Small beam bond test method for CFRP composites applied to concrete. Journal of Composites for Construction 2010;15:52–61.

[6] Tatar J, Hamilton HR. Comparison of laboratory and field environmental conditioning on FRP-concrete bond durability. Constr Build Mater 2016;122:525–36.

[7] Chen JF, Li XQ, Lu Y, May IM, Stratford TJ, O'Sullivan R, et al. A new test method for FRP-to-concrete bond behaviour under impact loading. The 12th International Symposium on Structural Engineering, Wuhan: 2012.

[8] Yao J, Teng JG, Chen JF. Experimental study on FRP-to-concrete bonded joints. Compos B Eng 2005;36:99–113.

[9] Bilotta A, di Ludovico M, Nigro E. FRP-to-concrete interface debonding: Experimental calibration of a capacity model. Compos B Eng 2011;42:1539–53.

[10] Hallonet A, Michel L, Ferrier E. Investigation of the bond behavior of flax FRP strengthened RC structures through double lap shear testing. Compos B Eng 2016;100:247–56.

[11] Shi J, Cao W, Wu Z. Effect of adhesive properties on the bond behaviour of externally bonded FRP-to-concrete joints. Compos B Eng 2019;177:107365.

[12] Chen JF, Yang ZJ, Holt GD. FRP or steel plate-to-concrete bonded joints: Effect of test methods on experimental bond strength. Steel and Composite Structures 2001;1:231–44.

[13] Tao Y, Chen JF. Concrete damage plasticity model for modeling FRP-to-concrete bond behavior. Journal of Composites for Construction 2015;19:4014026.

[14] Li X, Chen J-F, Lu Y, Yang Z. Modelling static and dynamic FRP-concrete bond behaviour using a local concrete damage model. Advances in Structural Engineering 2015;18:45–58.

[15] Xu T, He ZJ, Tang CA, Zhu WC, Ranjith PG. Finite element analysis of width effect in interface debonding of FRP plate bonded to concrete. Finite Elements in Analysis and Design 2015;93:30–41.

[16] Lin J, Wu Y, Smith ST. Width factor for externally bonded FRP-to-concrete joints. Constr Build Mater 2017;155:818–29.

[17] Pan J, Leung CKY, Asce M. Effect of Concrete Composition on FRP / Concrete Bond Capacity. Journal of Composites for Construction 2007;11:611–8.

[18] Mostofinejad D, Sanginabadi K, Eftekhar MR. Effects of coarse aggregate volume on CFRP-concrete bond strength and behavior. Constr Build Mater 2019;198:42–57.

[19] Mukhtar FM. Customized shear test for bond-slip characterization of EBR FRP-concrete system: Influence of substrate aggregate type. Compos B Eng 2019;163:606–21.

[20] Li YQ, Chen JF, Yang ZJ, Esmaeeli E, Sha W, Huang YJ. Effects of concrete heterogeneity on FRP-concrete bond behaviour: Experimental and mesoscale numerical studies. Compos Struct 2021;275:114436.

[21] Wang X, Yang ZJ, Yates JR, Jivkov AP, Zhang C. Monte Carlo simulations of mesoscale fracture modelling of concrete with random aggregates and pores. Constr Build Mater 2015;75:35–45.

[22] Hirsh TJ. Modulus of elasticity of concrete affected by elastic moduli of cement paste matrix and aggregate. ACI Journal Proceedings 1962;59:427–52.

[23] Zhang J, Wang Z, Yang H, Wang Z, Shu X. 3D meso-scale modeling of reinforcement concrete with high volume fraction of randomly distributed aggregates. Constr Build Mater 2018;164:350–61.

[24] Wriggers P, Moftah SO. Mesoscale models for concrete: Homogenisation and damage behaviour. Finite Elements in Analysis and Design 2006;42:623–36.

[25] Zhang Z, Song X, Liu Y, Wu D, Song C. Three-dimensional mesoscale modelling of concrete composites by using random walking algorithm. Compos Sci Technol 2017;149:235–45.

[26] Bandyopadhyaya R, Das A, Basu S. Numerical simulation of mechanical behaviour of asphalt mix. Constr Build Mater 2008;22:1051–8.

[27] Tülin A, Mustafa T, Tahir Ç. Effect of coarse aggregate size and matrix quality on ITZ and failure behavior of concrete under uniaxial compression. Cem Concr Compos 2004;26:633–8.

[28] Huang YJ, Yang Z, Ren W, Liu G, Zhang C. 3D meso-scale fracture modelling and validation of concrete based on in-situ X-ray Computed Tomography images using damage plasticity model. Int J Solids Struct 2015;67–68:340–52.

[29] BS 8110. Structural Use of Concrete—Part 1: Code of Practice for Design and Construction. British Standards Institution, London.; 1997.

[30] Eurocode 2: Design of concrete structures. 2004.

[31] Tan H, Huang Y, Liu C, Geubelle PH. The Mori-Tanaka method for composite materials with nonlinear interface debonding. Int J Plast 2005;21:1890–918.

[32] Mori T, Tanaka K. Average stress in matrix and average elastic energy of materials with misfitting inclusions. Acta Metallurgica 1973;21:571–4.

[33] Sideris KK, Manita P, Sideris K. Estimation of ultimate modulus of elasticity and Poisson ratio of normal concrete. Cem Concr Compos 2004;26:623–31.

[34] CEB-FIP Model Code 1990 : Design Code. London: Thomas Telford: 1993.

[35] Contrafatto L, Cuomo M, Gazzo S. A concrete homogenisation technique at meso-scale level accounting for damaging behaviour of cement paste and aggregates. Comput Struct 2016;173:1–18.

[36] ABAQUS. ABAQUS 6.11 user's manual. Providence, RI, USA: Dassault Systèmes; 2011.

[37] Huang YJ, Yang ZJ, Chen XW, Liu GH. Monte Carlo simulations of meso-scale dynamic compressive behavior of concrete based on X-ray computed tomography images. Int J Impact Eng 2016;97:102–15.

[38] Hordijk DA. Local approach to fatigue of concrete. Phd Theis. Ph.D Thesis. Delft University of Technology, 1991.

[39] Saenz LP. Discussion of equation for the stress-strain curve of concrete-by Desayi, P. and Krishan, S. Journal of the American Concrete Institute 1964;61:1229–35.

[40] De Borst R. Fracture in quasi-brittle materials: a review of continuum damage-based approaches. Eng Fract Mech 2002;69:95–112.

[41] Van Mier JGM. Strain-softening of concrete under multiaxial loading conditions. PhD. Thesis. Eindhoven University of Technology, 1984.

[42] Vonk RA. Softening of concrete loaded in compression. PhD. Thesis. Eindhoven University of Technology, 1992.

[43] Feenstra PH. Computational aspects of biaxial stress in plain and reinforced concrete. 1993.

[44] Markeset G, Hillerborg A. Softening of concrete in compression-localization and size effect. Cem Concr Res 1995;25:702–8.

[45] Nakamura H, Higai T. Compressive fracture energy and fracture zone length of concrete. Modelling of Inelastic Behavior of RC Structures under Seismic Loads 2001:471–87.

[46] Alfarah B, López-Almansa F, Oller S. New methodology for calculating damage variables evolution in Plastic Damage Model for RC structures. Eng Struct 2017;132:70–86.

[47] Krätzig WB, Pölling R. An elasto-plastic damage model for reinforced concrete with minimum number of material parameters. Comput Struct 2004;82:1201–15.

[48] Lubliner J, Oliver J, Oller S, Oñate E. A plastic-damage model for concrete. Int J Solids Struct 1989;25:299–326.

[49] Li Q, Ansari F. Mechanics of damage and constitutive relationships for high-strength concrete in triaxial compression. J Eng Mech 1999;125:1–10.

[50] Zhou R, Song Z, Lu Y. 3D mesoscale finite element modelling of concrete. Comput Struct 2017;192:96–113.

[51] Huang YJ, Yang ZJ, Liu GH, Chen XW. An efficient FE–SBFE coupled method for mesoscale cohesive fracture modelling of concrete. Comput Mech 2016;58:635–55.

[52] Ren W, Yang Z, Sharma R, Zhang C, Withers PJ. Two-dimensional X-ray CT image based meso-scale fracture modelling of concrete. Eng Fract Mech 2015;133:24–39.

[53] Baltay P, Gjelsvik A. Coefficient of friction for steel on concrete at high normal stress. Journal of Materials in Civil Engineering 1990;2:46–9.

[54] van Vliet MRA, van Mier JGM. Experimental investigation of concrete fracture under uniaxial compression. Mechanics of Cohesive-frictional Materials: An International Journal on Experiments, Modelling and Computation of Materials and Structures 1996;1:115–27.

[55] Chen JF, Teng JG. Anchorage strength models for FRP and steel plates bonded to concrete. Journal of Structural Engineering 2001;127:784–91.

[56] Chen GM, Teng JG, Chen JF, Xiao QG. Finite element modeling of debonding failures in FRP-strengthened RC beams: A dynamic approach. Comput Struct 2015;158:167–83.

[57] Zhang P, Lei D, Ren Q, He J, Shen H, Yang Z. Experimental and numerical investigation of debonding process of the FRP plate-concrete interface. Constr Build Mater 2020;235:117457.

[58] Li Y, Yang Z, Zhang Z, Peng C, Lin M. A multiscale experimental study of CFRP-UHPFRC interfacial bond behaviour: Failure mechanisms and a fibre volume dependent bond-slip law. Structures 2024;63:106322.

[59] An F. Modelling of FRP-concrete interfacial bond behaviour. PhD Thesis. The University of Edinburgh, 2015.

[60] Birtel V, Mark P. Parameterised finite element modelling of RC beam shear failure. Abaqus User’s Conference 2006:95–108.

[61] Ali-Ahmad Mo, Subramaniam K, Ghosn M. Experimental investigation and fracture analysis of debonding between concrete and FRP sheets. J Eng Mech 2006;132:914–23.

[62] Wu ZS, Yuan H, Hiroyuki Y, Toshiyuku K. Experimental/analytical study on interfacial fracture energy and fracture propagation along FRP-concrete interface. ACI International 2001;SP-201-8:133–52.

[63] Guo Z. Principles of reinforced concrete. Butterworth-Heinemann; 2014.